

Probing Intergalactic Magnetic Fields with Simulations of Electromagnetic Cascades

Rafael Alves Batista^{1,*}, Andrey Saveliev^{2,3,†}, Günter Sigl^{2,‡}, Tanmay Vachaspati^{4,§}

¹*University of Oxford, Department of Physics - Astrophysics,
Denys Wilkinson Building, Keble Road, Oxford OX1 3RH, United Kingdom*

²*Universität Hamburg, II. Institute for Theoretical Physics,
Luruper Chaussee 149, 22761 Hamburg, Germany*

³*Russian Academy of Sciences, Keldysh Institute of Applied Mathematics,
Miusskaya sq. 4, 125047 Moscow, Russian Federation*

⁴*Arizona State University, Physics Department, 650 E. Tyler Mall, Tempe, AZ 85287, United States of America*

We determine the effect of intergalactic magnetic fields on the distribution of high energy gamma rays by performing three-dimensional Monte Carlo simulations of the development of gamma-ray-induced electromagnetic cascades in the magnetized intergalactic medium. We employ the so-called “Large Sphere Observer” method to efficiently simulate blazar gamma ray halos. We study magnetic fields with a Batchelor spectrum and with maximal left- and right-handed helicities. We also consider the case of sources whose jets are tilted with respect to the line of sight. We verify the formation of extended gamma ray halos around the source direction, and observe spiral-like patterns if the magnetic field is helical. We apply the Q -statistics to the simulated halos to extract their spiral nature and also propose an alternative method, the S -statistics. Both methods provide a quantitative way to infer the helicity of the intervening magnetic fields from the morphology of individual blazar halos for magnetic field strengths $B \gtrsim 10^{-15}$ G and magnetic coherence lengths $L_c \gtrsim 100$ Mpc. We show that the S -statistics has a better performance than the Q -statistics when assessing magnetic helicity from the simulated halos.

I. INTRODUCTION

The origin, strength and structure of intergalactic magnetic fields (IGMF) remain a mystery up to the present day. Possible mechanisms to explain cosmic magnetogenesis may be divided into two main categories: cosmological scenarios predict that magnetic fields were generated through processes taking place in the early universe, such as inflation [1–4], electroweak [5–8] or QCD phase transitions [9–12], and leptogenesis [13, 14], among others; in astrophysical scenarios the fields would be created during the later stages of evolution of the universe, for example during structure formation [15] or even thereafter [16].

Measurements of IGMF are rather difficult due to their low magnitude. Common methods to estimate the strength of IGMF are indirect and include the well-known Faraday rotation measurements which yield upper limits of the order of a few nG [19]. Lower bounds, $B \gtrsim 10^{-17}$ G, have been obtained by several authors using gamma-ray-induced electromagnetic cascades in the intergalactic space [19–26]. These lower bounds are controversial because of the claims [27–31] that the development of the cascade is suppressed by plasma instabilities that arise from interactions with the intergalactic medium. On the other hand, recent direct observations [32] and PIC simulations [33] of cascades suggest that plasma instabilities are not operative and that the orig-

inal bounds hold. We expect that future analyses will clarify the role, if any, of plasma instabilities in the development of the electromagnetic cascade.

Magnetic fields can carry helicity (\mathcal{H}), which is defined as

$$\mathcal{H} = \int \mathbf{A} \cdot \mathbf{B} d^3r, \quad (1)$$

where \mathbf{A} is the magnetic vector potential and $\mathbf{B} = \nabla \times \mathbf{A}$ is the magnetic field. Since magnetic helicity affects the dynamical evolution of magnetic fields, an indirect way to measure magnetic helicity is to measure the magnetic field power spectrum and compare it with the evolution seen in magnetohydrodynamical (MHD) simulations [34–36].

The magnetic helicity, \mathcal{H} , being given by a volume integral is a global quantity, and hence is not directly measurable unless additional assumptions are invoked. The integrand in Eq. (1), $\mathbf{A} \cdot \mathbf{B}$, is local but not measurable because it is gauge dependent. Instead, local measurements can measure the “current helicity” which is defined as $\mathbf{B} \cdot \nabla \times \mathbf{B}$ and this will be our focus. Early work based on the propagation of cosmic rays to measure the helical part of the magnetic field correlation function [37] also yields a measure of the magnetic current helicity.

More recently, it has been proposed that helicity can leave characteristic parity-odd imprints on the arrival directions of gamma rays that are the result of gamma-ray-induced electromagnetic cascades [32, 38–41]. In particular, Long & Vachaspati [41] have carried out a thorough analysis of the morphology of the arrival directions of gamma rays using a semi-analytical approach, but without including the stochasticity of the magnetic field or the cascade process. Hence, a full Monte Carlo approach

*E-mail: rafael.alvesbatista@physics.ox.ac.uk

†E-mail: andrey.saveliev@desy.de, *corresponding author*

‡E-mail: guenter.sigl@desy.de

§E-mail: tvachasp@asu.edu

and three-dimensional simulations are needed in order to confirm or refute their findings and provide a solid basis for further analyses.

The observation of helical primordial magnetic fields has profound implications for particle physics and the early universe. Scenarios in which the cosmological matter-antimatter asymmetry is generated dynamically are found to also produce helical magnetic fields [42]. The handedness of the field is related to details of the matter-genesis scenario [13, 42]. If the observed magnetic fields are coherent on very large scales, they may have been produced at the initial epoch, perhaps during an inflation [1, 2]. Helicity on these scales would indicate the presence of certain parity violating interactions in the fundamental Lagrangian [43].

In the present work we perform simulations of the propagation of gamma rays in both helical and non-helical IGMF. This paper is structured as follows: first, we discuss the theory and implementation of simulations of electromagnetic cascades in Sec. II; in Sec. III we apply our approach to different magnetic field configurations, focusing in particular on the role of magnetic helicity (Sec. III C - III D); in Sec. IV we discuss the results, draw our conclusions and give a short outlook.

II. SIMULATIONS OF ELECTROMAGNETIC CASCADES IN THE INTERGALACTIC MEDIUM

A. Interactions and Energy Losses

The basic physics underlying the development of electromagnetic cascades induced by high energy gamma rays from blazars is well-known [44, 45]. A gamma ray emitted by a blazar interacts with photons from the diffuse extragalactic background radiation fields producing an electron-positron pair. The electrons¹ then upscatter photons of the cosmic microwave background to high energies in a process known as inverse Compton scattering (ICS). The electrons continue to upscatter photons until their energy diminishes. The upscattered photons can produce yet more electron-positron pairs until the energy of the photon drops below the threshold for pair production. We should therefore observe the blazar source as well as gamma rays originating from the cascade process, unless magnetic fields bend the electron trajectories sufficiently away from the line of sight.

To perform three-dimensional simulations of the development of gamma-ray-induced electromagnetic cascades in the IGM, we have modified the CRPropa 3 [46] code, commonly used for ultra-high energy cosmic ray propagation. Taking advantage of the modular structure of the code and the flexibility to handle custom magnetic

field configurations, we have implemented relevant interactions for gamma rays and electrons in the energy range of interest ($1 \text{ GeV} \lesssim E \lesssim 1 \text{ PeV}$). Relevant interactions are pair production by gamma rays and inverse Compton scattering by electrons. Adiabatic losses due to the expansion of the universe are also taken into account. Synchrotron losses, albeit small in this energy range, are considered as well, for the sake of completeness.

Particles are propagated step-by-step. Within each step the probability of a given interaction to occur is computed using tabulated values for the interaction rate. If the particle is charged, deflections due to magnetic fields are calculated by integrating the equations of motion. By doing so, we are adopting a three-dimensional Monte Carlo approach for the propagation.

Interaction rates for pair production and inverse Compton scattering are calculated following the implementation used in the Elmag code [47], and defined as the inverse of the mean free path λ . They are tabulated for the CMB and various models of extragalactic background light (EBL) at different redshifts as follows² [47]:

$$R(E, z) \equiv \lambda^{-1}(E, z) = \frac{1}{8E^2} \int_0^\infty d\varepsilon \int_{s_{\min}}^{s_{\max}} ds \frac{n(\varepsilon, z)}{\varepsilon^2} F_{\text{int}}(s), \quad (2)$$

where E is the energy of the interacting particle (electron, positron or photon), $n(\varepsilon, z)$ is the comoving spectral density distribution of photons with energy ε at redshift z , s denotes the center of mass energy in the kinematic range $s_{\min} \leq s \leq s_{\max}$, and F_{int} is a function that depends on the interaction in question.

In the case of pair production $F_{\text{int}} = F_{\text{PP}}$ is

$$F_{\text{PP}}(s) = s\sigma_{\text{PP}}(s), \quad (3)$$

where $\sigma_{\text{PP}}(s)$ is the cross section for pair production, and $s = 2E\varepsilon(1 - \cos\theta)$, with $0 \leq \theta \leq \pi$ being the angle between the gamma ray of energy E and the background photon of energy ε . The values of s range from $s_{\min} = 4m_e^2$ to $s_{\max} = 4E\varepsilon_{\max}$, where ε_{\max} is the cutoff energy for the photon field, assumed to be approximately 0.1 eV for the CMB and 15 eV for the EBL.

For inverse Compton scattering $F_{\text{int}} = F_{\text{ICS}}$ is given by

$$F_{\text{ICS}}(s) = \frac{1}{\beta} \sigma_{\text{ICS}}(s - m_e^2), \quad (4)$$

with $\beta = (1 - m_e^2/E^2)^{\frac{1}{2}}$. The center of mass energies in this case are $s = m_e^2 + 2E\varepsilon(1 - \beta \cos\theta)$, for $s_{\min} \leq s \leq s_{\max}$, with $s_{\min} = m_e^2$ and $s_{\max} = m_e^2 + 2E\varepsilon_{\max}(1 + \beta)$.

Cross sections for these interactions are well-known (see e.g. [47, 48]). The spectral density distribution of the

¹ Hereafter we will collectively refer to electrons and positrons simply as “electrons”.

² Unless otherwise stated, in this section we use “natural units” in which $\hbar = c = 1$.

cosmic microwave background (CMB) can be described as a black-body. The EBL is model-dependent. For this particular work we adopt the lower limit EBL model of Kneiske & Dole [49].

Synchrotron losses are given by

$$\frac{dE}{dx} = \frac{m_e^2 \chi^2}{(1 + 4.8(1 + \chi) \ln(1 + 1.7\chi) + 3.4\chi^2)^{2/3}}, \quad (5)$$

following Ref. [47]. Here m_e is the electron mass, χ is

$$\chi \equiv \frac{|\mathbf{p} \times \mathbf{B}|}{m_e B_0}, \quad (6)$$

with $B_0 = 4.1 \times 10^{13}$ G, and \mathbf{B} the magnetic field vector acting on an electron with momentum \mathbf{p} .

Adiabatic losses due to the expansion of the universe are given by

$$-\frac{1}{E} \frac{dE}{dx} = \frac{H(t)}{c} = \frac{H_0}{c} \sqrt{\Omega_m(1+z)^3 + \Omega_\Lambda}, \quad (7)$$

with $H_0 \equiv H(0) \simeq 70$ km/s/Mpc designating the Hubble constant at present time, $\Omega_m \simeq 0.3$ being the density of matter, and $\Omega_\Lambda \simeq 0.7$ being the density of dark energy, assuming the standard Λ CDM cosmological model.

In our simulations we consider a monochromatic source and all emitted gamma rays are assumed to have an energy of 10 TeV. Photons from the source with energies much smaller than this will be below the threshold for creating a cascade, while photons with much higher energies will have a diminished flux.

B. Sampling of Helical Magnetic Fields

In order to run a simulation for a given magnetic field scenario or, more specifically, for a given magnetic field (and magnetic helicity) spectrum, one has to sample a magnetic field grid which then may be used as input. This procedure is explained in the following using the formalism of [50].

The aim is to decompose the magnetic field into modes of the divergence-free eigenfunctions \mathbf{K}^\pm of the Laplace operator which for a specific wave vector \mathbf{k} are given by³

$$\mathbf{K}^\pm(\mathbf{k}) = \mathbf{e}^\pm(\mathbf{k}) e^{i\mathbf{k} \cdot \mathbf{x}} \equiv \frac{\mathbf{e}_1(\mathbf{k}) \pm i\mathbf{e}_2(\mathbf{k})}{\sqrt{2}} e^{i\mathbf{k} \cdot \mathbf{x}}, \quad (8)$$

where $(\mathbf{e}_1, \mathbf{e}_2, \mathbf{e}_3)$ is a right-handed orthonormal system of real unit vectors with $\mathbf{e}_3 = \mathbf{k}/k \equiv \hat{\mathbf{k}}$. In order to obtain \mathbf{e}_1 and \mathbf{e}_2 we chose a fixed arbitrary vector $\mathbf{n}_0 \nparallel \mathbf{k}$ with which we calculate

$$\mathbf{e}_1 \equiv \frac{\mathbf{n}_0 \times \hat{\mathbf{k}}}{|\mathbf{n}_0 \times \hat{\mathbf{k}}|}, \quad \mathbf{e}_2 \equiv \frac{\hat{\mathbf{k}} \times \mathbf{e}_1}{|\hat{\mathbf{k}} \times \mathbf{e}_1|}. \quad (9)$$

With these definitions the \mathbf{K}^\pm fulfil the following relations [50]:

$$\nabla \cdot \mathbf{K}^\pm = 0, \quad \nabla \times \mathbf{K}^\pm = \pm k \mathbf{K}^\pm. \quad (10)$$

Considering these relations the magnetic field with $\nabla \cdot \mathbf{B} = 0$ or, in Fourier space, $\mathbf{k} \cdot \tilde{\mathbf{B}}(\mathbf{k}) = 0$ may be decomposed as

$$\mathbf{B}(\mathbf{x}) = \int \left[\tilde{B}^+(\mathbf{k}) \mathbf{K}^+(\mathbf{k}) + \tilde{B}^-(\mathbf{k}) \mathbf{K}^-(\mathbf{k}) \right] \frac{d^3 k}{(2\pi)^3}, \quad (11)$$

for which, in order for $\mathbf{B}(\mathbf{x})$ to be real, the condition

$$\begin{aligned} \tilde{B}^+(\mathbf{k}) \mathbf{e}^+(\mathbf{k}) + \tilde{B}^-(\mathbf{k}) \mathbf{e}^-(\mathbf{k}) \\ = \tilde{B}^+(-\mathbf{k})^* \mathbf{e}^+(-\mathbf{k})^* + \tilde{B}^-(-\mathbf{k})^* \mathbf{e}^-(-\mathbf{k})^* \end{aligned} \quad (12)$$

must hold. A possible realization of this condition is

$$\tilde{B}^\pm(\mathbf{k}) \mathbf{e}^\pm(\mathbf{k}) = \tilde{B}^\pm(-\mathbf{k})^* \mathbf{e}^\pm(-\mathbf{k})^*, \quad (13)$$

which can be fulfilled by setting

$$\tilde{B}^\pm(\mathbf{k}) = \tilde{B}^\pm(-\mathbf{k})^*, \quad (14)$$

which we are going to use in the following. Together with (8) and (13) this leads to

$$\mathbf{e}^\pm(\mathbf{k}) = \mathbf{e}^\pm(-\mathbf{k})^*, \quad (15)$$

and thus

$$\mathbf{e}_1(\mathbf{k}) = -\mathbf{e}_1(-\mathbf{k}), \quad \mathbf{e}_2(\mathbf{k}) = \mathbf{e}_2(-\mathbf{k}). \quad (16)$$

The \tilde{B}^\pm may be obtained from the given spectra using the relations [50]

$$\begin{aligned} \frac{1}{8\pi} \langle |\mathbf{B}(\mathbf{x})|^2 \rangle &= \int \left[|\tilde{B}^+(\mathbf{k})|^2 + |\tilde{B}^-(\mathbf{k})|^2 \right] \frac{k^2 dk}{16\pi^3} \\ &\equiv \int E_B(k) d \ln k \end{aligned} \quad (17)$$

and

$$\begin{aligned} \langle \mathbf{A}(\mathbf{x}) \cdot \mathbf{B}(\mathbf{x}) \rangle &= \int \left[|\tilde{B}^+(\mathbf{k})|^2 - |\tilde{B}^-(\mathbf{k})|^2 \right] \frac{k dk}{2\pi^2} \\ &\equiv \int H_B(k) d \ln k, \end{aligned} \quad (18)$$

where \mathbf{A} is the vector potential and E_B and H_B are the spectra of the magnetic energy density and the magnetic helicity density, respectively. It should be noted here that, while (18) is defined in terms of the vector potential \mathbf{A} , it is also possible to relate it to the current helicity as described in Appendix A.

E_B and H_B are related to each other through the inequality [51]

$$\frac{k}{8\pi} |H_B(k)| \leq E_B(k) \quad (19)$$

³ We adopt CGS units in this section.

which may be also expressed as

$$H_B(k) = f_H(k) \frac{8\pi}{k} E_B(k) \quad (20)$$

with $-1 \leq f_H(k) \leq 1$.

Numerical and analytical analyses [36, 52] show that E_B is a power-law for small k , *i.e.*

$$E_B \propto k^\alpha, \quad (21)$$

with $\alpha = 5$. This power-law behavior for E_B is also known as the Batchelor spectrum.

In our numerical analysis with stochastic magnetic fields of Sec. III C, we will use magnetic fields with the spectrum

$$E_B \propto \begin{cases} k^5, & k \leq 2\pi/L_{\min}, \\ 0, & k > 2\pi/L_{\min}, \end{cases} \quad (22)$$

where, for a correlation length $L_c = 120$ Mpc, $L_{\min} = 8L_c/5 = 192$ Mpc is the cutoff scale (cf. Eq. (28) below).

Finally, solving (17) and (18) for $|\tilde{B}^\pm|^2$ gives

$$\begin{aligned} |\tilde{B}^\pm|^2 &= \frac{8\pi^3}{k^3} \left[E_B(k) \pm \frac{k}{8\pi} H_B(k) \right] \\ &= \left(\frac{2\pi}{k} \right)^3 [1 \pm f_H(k)] E_B(k). \end{aligned} \quad (23)$$

With these considerations the procedure for sampling a magnetic field for given spectra E_B and H_B on a grid in x -space is the following: first, for each \mathbf{k} in the Fourier-transformed k -space a value for the norm of $\tilde{B}(k)$ is generated from a normal distribution with mean value $\mu = 0$ and standard deviation $\sigma = 2(2\pi/k)^3 E_B(k)$ as follows from (23) with $f_H = \pm 1$. Next, we include a random phase factor

$$\tilde{B}^\pm(\mathbf{k}) = |\tilde{B}^\pm(\mathbf{k})| [\cos \theta^\pm(\mathbf{k}) + i \sin \theta^\pm(\mathbf{k})], \quad (24)$$

where $\theta^\pm(\mathbf{k})$ are random phases distributed uniformly on $[0; 2\pi)$. Once we have $\tilde{B}^\pm(\mathbf{k})$, we use Eq. (14) to find $\tilde{B}^\pm(-\mathbf{k})$. These $\tilde{B}^\pm(\mathbf{k})$ can then be plugged into (11) to obtain the value for $\mathbf{B}(\mathbf{x})$ at a given \mathbf{x} .

As sometimes it is more convenient to have $\tilde{\mathbf{B}}(\mathbf{k})$ given in terms of the real and imaginary parts, we use Eq. (8) to write it down in the form

$$\begin{aligned} \tilde{\mathbf{B}}(\mathbf{k}) &= \tilde{B}^+(\mathbf{k}) \mathbf{e}^+(\mathbf{k}) + \tilde{B}^-(\mathbf{k}) \mathbf{e}^-(\mathbf{k}) \\ &= \frac{1}{\sqrt{2}} \left\{ \left[\left(|\tilde{B}^+(\mathbf{k})| \cos \theta^+ + |\tilde{B}^-(\mathbf{k})| \cos \theta^- \right) \mathbf{e}_1 + \left(-|\tilde{B}^+(\mathbf{k})| \sin \theta^+ + |\tilde{B}^-(\mathbf{k})| \sin \theta^- \right) \mathbf{e}_2 \right] \right. \\ &\quad \left. + i \left[\left(|\tilde{B}^+(\mathbf{k})| \sin \theta^+ + |\tilde{B}^-(\mathbf{k})| \sin \theta^- \right) \mathbf{e}_1 + \left(|\tilde{B}^+(\mathbf{k})| \cos \theta^+ - |\tilde{B}^-(\mathbf{k})| \cos \theta^- \right) \mathbf{e}_2 \right] \right\}. \end{aligned} \quad (25)$$

III. RESULTS

In this section we present the results. Some preliminary considerations regarding the setup of simulations should first be made.

We use the Large Sphere Observer approach which is a computationally efficient method for studying cosmic and gamma rays from a single source [53, 54]. It is defined by the fact that this source is located in the center of a sphere which has a radius equal to D_s , the distance from the source to the observer. Hence, if a particle crosses the sphere from the inside to the outside, it is flagged ‘detected’. This will henceforth be called a ‘hit’ and it corresponds to the particle reaching the observer.

The source can emit gamma rays either within a jet or isotropically. Due to the choice of a large sphere as an observer, all events above a given energy threshold (here we use 1.5 GeV) are detected. Moreover, we can easily

select a subset of the events and consider an arbitrary emission pattern, such as a jet of arbitrary half-opening angle Ψ , or an emission around an arbitrary direction tilted with respect to the line of sight.

Simple geometrical considerations allow us to correct the arrival directions on the large sphere to mimic Earth’s field of view. In the sky maps presented in this work, for each hit, the corresponding coordinate system of the observer is placed such that its origin is located at the position of the hit while the z axis points towards the source, *i.e.* in the direction of the center of the sphere. In order to determine the directions of the x and y axes, we take a “global” reference frame at a fixed point of the sphere and parallel-transport it along a geodesic to the location of the hit. Then the spherical angles of the event are measured in the local frame located at the hit point.

While the “Large Sphere Observer” method is economical as no photons are wasted, one possible concern is that in a realistic set-up most photons would indeed be wasted

and the actual halo morphology would be sensitive to the absent photons. However, our results in the test case of a uniform magnetic field correlate well with analytic simulations [41], giving us confidence in the method.

The magnetic field (except for the uniform case) is sampled in a grid with 1000^3 cells, where each cell has a size of ~ 10 Mpc.

A. Comparison with Analytic Estimates

For a gamma ray emitted at TeV energy E_{TeV} and observed at an energy E_γ , originating from a source (blazar in our case) located at redshift z_s and distance D_s , traversing a magnetic field of strength B , the expected average angular arrival direction is [19]

$$\theta(E_\gamma) \simeq 0.05^\circ \kappa (1 + z_s)^{-4} \times \left(\frac{B}{\text{fG}}\right) \left(\frac{E_\gamma}{0.1 \text{ TeV}}\right)^{-1} \left(\frac{D_s}{\text{Gpc}}\right)^{-1} \left(\frac{E_{\text{TeV}}}{10 \text{ TeV}}\right)^{-1} \quad (26)$$

This formula is only a rough estimate where κ is a factor close to unity, $\kappa \simeq 1$, which varies slightly with the EBL model chosen. Furthermore, this equation is only valid if the coherence length (L_c) of the field is much larger than the propagation length of electrons before they upscatter photons via inverse Compton. This is always true in our simulations because the propagation length is of the order of 30 kpc, whereas the minimum coherence length is 10 Mpc.

In order to compare our results with Eq. (26), we simulate the propagation of gamma rays with initial energies $E_{\text{TeV}} = 10$ TeV, distance $D_s = 1$ Gpc ($z_s \simeq 0.25$), emitted in a collimated jet along the line of sight assuming stochastic magnetic fields with strength of $B = 10^{-16}$ G and $B = 10^{-15}$ G. The maps containing the arrival directions are shown in the top panel of Fig. 1.

We have compared the deflections obtained from the simulations with the theoretical prediction of Eq. (26). This is shown in the bottom panel of Fig. 1. The results show a good agreement with the expected deflections. Differences are due to the nature of the analytic formula itself, which has been derived in [19] using various simplifying assumptions. Furthermore, as has been pointed out in Ref. [19], the deflection angle is highly sensitive to the particular EBL model used. In particular, for the EBL model used here (Kneiske & Dole [49]), we expect $\kappa \approx 2.3$. As pointed out in Ref. [19], $0.3 \lesssim \kappa \lesssim 3.0$ for typical EBL models found in the literature.

B. Uniform Magnetic Fields

We now consider a simple scenario with a uniform magnetic field. By definition, a uniform magnetic field has a preferred direction, and therefore one has to distinguish among three general cases depending on the orientation of the magnetic field with respect to the axis of

the jet: parallel, perpendicular, and intermediate orientation. The jet direction is assumed to be along the line of sight.

In Fig. 2 these different cases are shown for a magnetic field of strength 10^{-15} G, assuming that the gamma rays are emitted in a jet with a half-opening angle of 5° and with energy $E_{\text{TeV}} = 10$ TeV. The results for the three cases with a specific focus on their energy dependence are shown in Fig. 2.

The results for the first case, in which the magnetic field is parallel to the jet axis, are rather intuitive and are shown in the upper left panel of Fig. 2. One can see that there is only one possible arrival direction, face-on, *i.e.* $\theta = 0^\circ$, which means that only photons produced by electrons created with momenta parallel to the magnetic field lines, and thus not influenced by the Lorentz force, can reach the observer. Any electron that deviates from the line of sight will have a trajectory that leaves the plane spanned by the line of sight and the velocity direction of the initial TeV photon and will not reach the observer.

The second case, shown in the top right panel of Fig. 2, has a magnetic field perpendicular to the line of sight. Here only photons arriving in a plane perpendicular to the magnetic field are detected. This means that the parent-electrons of these photons describe circular motion in this same plane. If an electron has a velocity component *parallel* to the magnetic field, it is initially directed away from the line of sight, and there is no component of the Lorentz force that can bend it back towards the observer.

In the case of an intermediate orientation of the magnetic field, illustrated through the bottom panel of Fig. 2 for a tilt angle of 45° (left) and 75° (right), we obtain results between the two extreme cases previously discussed, as expected. It is interesting to notice that the patterns are now smeared out since electrons from a range of directions can be directed towards the observer. Still, the dilution of the signal is small compared to the actual deflection, and hence this can be observed. Therefore, relevant information can still be extracted from sky maps by using the morphology of the arrival directions.

C. Stochastic Helical Magnetic Fields

Now we introduce magnetic helicity to the simulations. The source is assumed to have a half opening angle $\Psi = 5^\circ$. We take the field to be stochastic with a Batchelor spectrum as in Eq. (22). As we are assuming the maximal helical case, *i.e.* $f_H = \pm 1$, this also fixes the spectrum of $H_B(k)$ according to Eq. (20). The field has an average field strength of $B_{\text{rms}} = 10^{-15}$ G and a correlation length of $L_c \simeq 120$ Mpc. Here, B_{rms}^2 can be extracted from

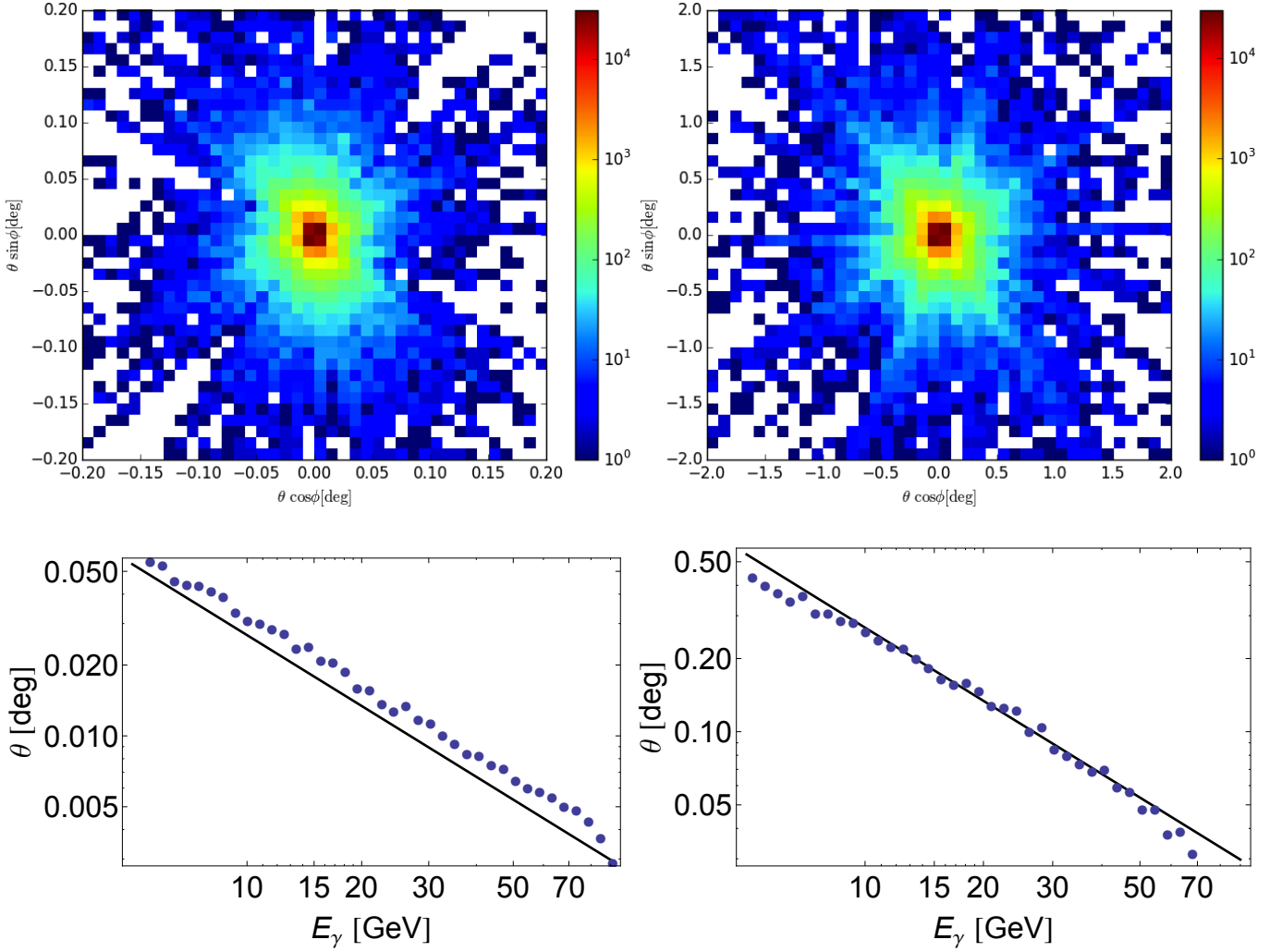


FIG. 1: Arrival directions of photons from a monochromatic TeV blazar emitting gamma rays with energies $E_{\text{TeV}} = 10$ TeV in a collimated jet, in the energy range of 1-100 GeV, projected onto a plane, are shown in the upper row; the color scale indicates the number of photons per bin. The deflection angle (θ) of observed gamma rays as a function of the energy are presented in the bottom row. The magnetic field is stochastic with a spectrum according to (21) and a mean field strength of 10^{-15} G (left column) and 10^{-16} G (right column); blue dots correspond to simulation results and the black line represents the analytical prediction using Eq. (26).

Eq. (17) by setting

$$\begin{aligned} B_{\text{rms}}^2 &\equiv \langle |\mathbf{B}(\mathbf{x})|^2 \rangle = \frac{1}{(2\pi)^3} \int |\tilde{B}(\mathbf{k})|^2 d^3k \\ &= 8\pi \int E_B(k) d \ln k, \end{aligned} \quad (27)$$

while L_c is defined by [55]

$$\begin{aligned} L_c &= \frac{1}{(2\pi)^3} \frac{\pi}{B_{\text{rms}}^2} \int |\tilde{B}(\mathbf{k})|^2 k^{-1} d^3k \\ &= \frac{8\pi^2}{B_{\text{rms}}^2} \int E_B(k) k^{-1} d \ln k, \end{aligned} \quad (28)$$

such that for the E_B defined in (22) we have $L_c \simeq 5L_{\text{min}}/8$, where L_{min} is the cutoff scale.

We have simulated the propagation of gamma rays with initial energy $E_{\text{TeV}} = 10$ TeV in the presence of stochastic magnetic fields with maximally negative ($f_H = -1$), zero ($f_H = 0$) and maximally positive ($f_H = +1$) helicities⁴. To simulate 10^5 photons in our standard scenario described above, *i.e.* with $D_s = 1$ Gpc and $B = 10^{-15}$ G, the current version of the code takes ~ 8 hours on 64 cores at 2300 MHz.

The actual values of the helicities for the whole sim-

⁴ We could generate the $f_H = -1$ gamma ray distribution by a parity reversal of the $f_H = +1$ plot. However, we simulate the two cases independently to show two different stochastic realizations.

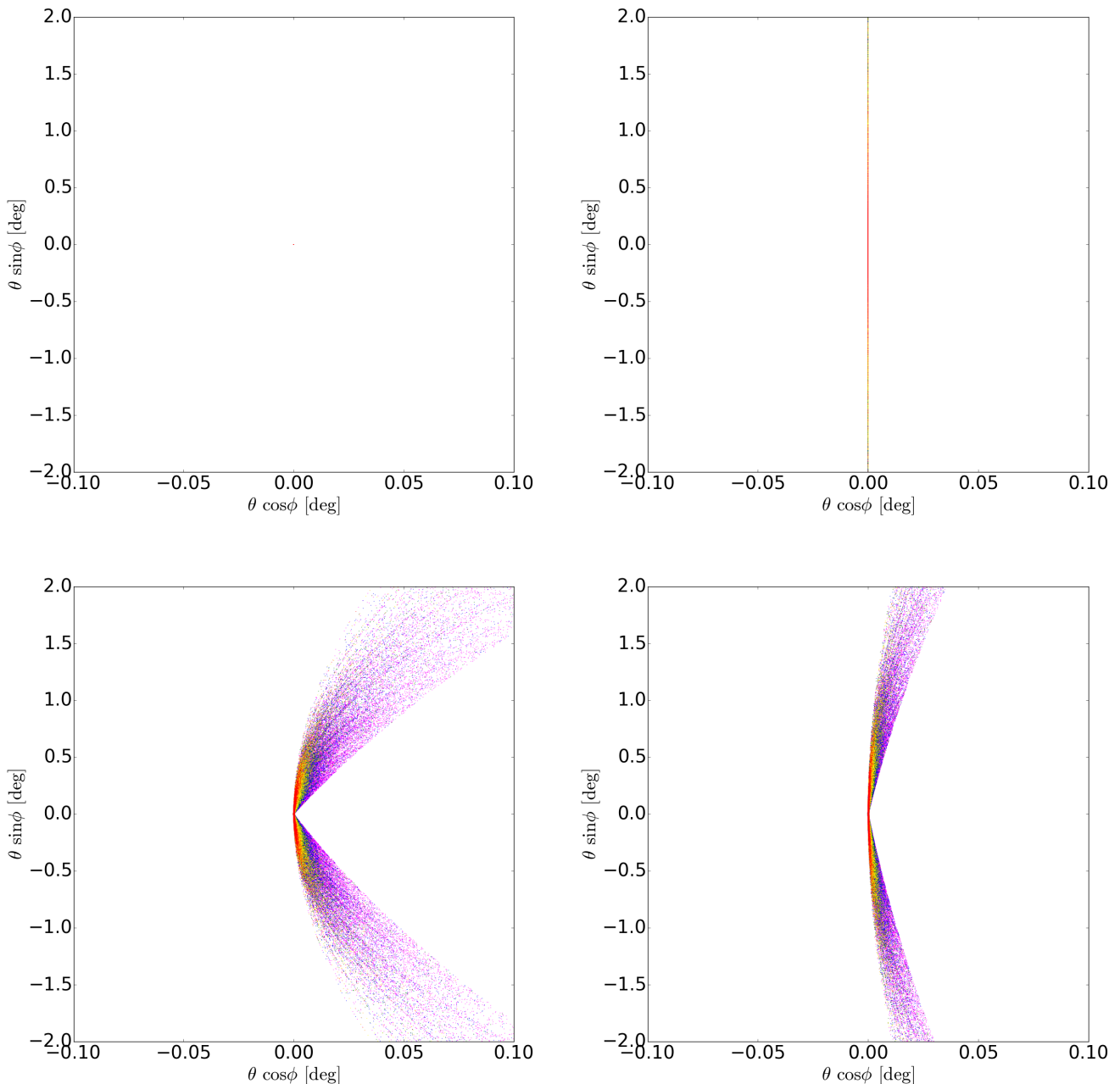


FIG. 2: Energy-dependent sky maps for a uniform magnetic field with $B = 10^{-15}$ G. We show the cases of a tightly collimated jet with magnetic field parallel (top left), perpendicular (top right), and tilted by 45 deg (bottom left) and 75 deg (bottom right) to the blazar jet direction which is taken to be along the line of sight. The different colors represent the following energy ranges: 5 – 10 GeV (magenta), 10 – 15 GeV (blue), 15 – 20 GeV (green), 20 – 30 GeV (yellow), 30 – 50 GeV (orange), 50 – 100 GeV (red).

ulation box as well as along the line of sight are shown in Fig. 5, in order to illustrate to which extent statistics play a role. As one can see, both for the whole grid as well as just along the line of sight, which is more important to judge about the statistical significance for a given case, the helicity distribution locally corresponds to the sign it has been assigned. Furthermore, from the panel

on the right, one can see that for these particular realizations, for $f_H = +1$ the absolute magnitude of $\mathbf{B} \cdot (\nabla \times \mathbf{B})$ is high close to the source and low close to the observer, while for $f_H = -1$ it stays roughly equal along the propagation path. We can understand the qualitatively similar patterns for $f_H = \pm 1$, *i.e.* both patterns are spirals with similar twist, by noting that pair production on average

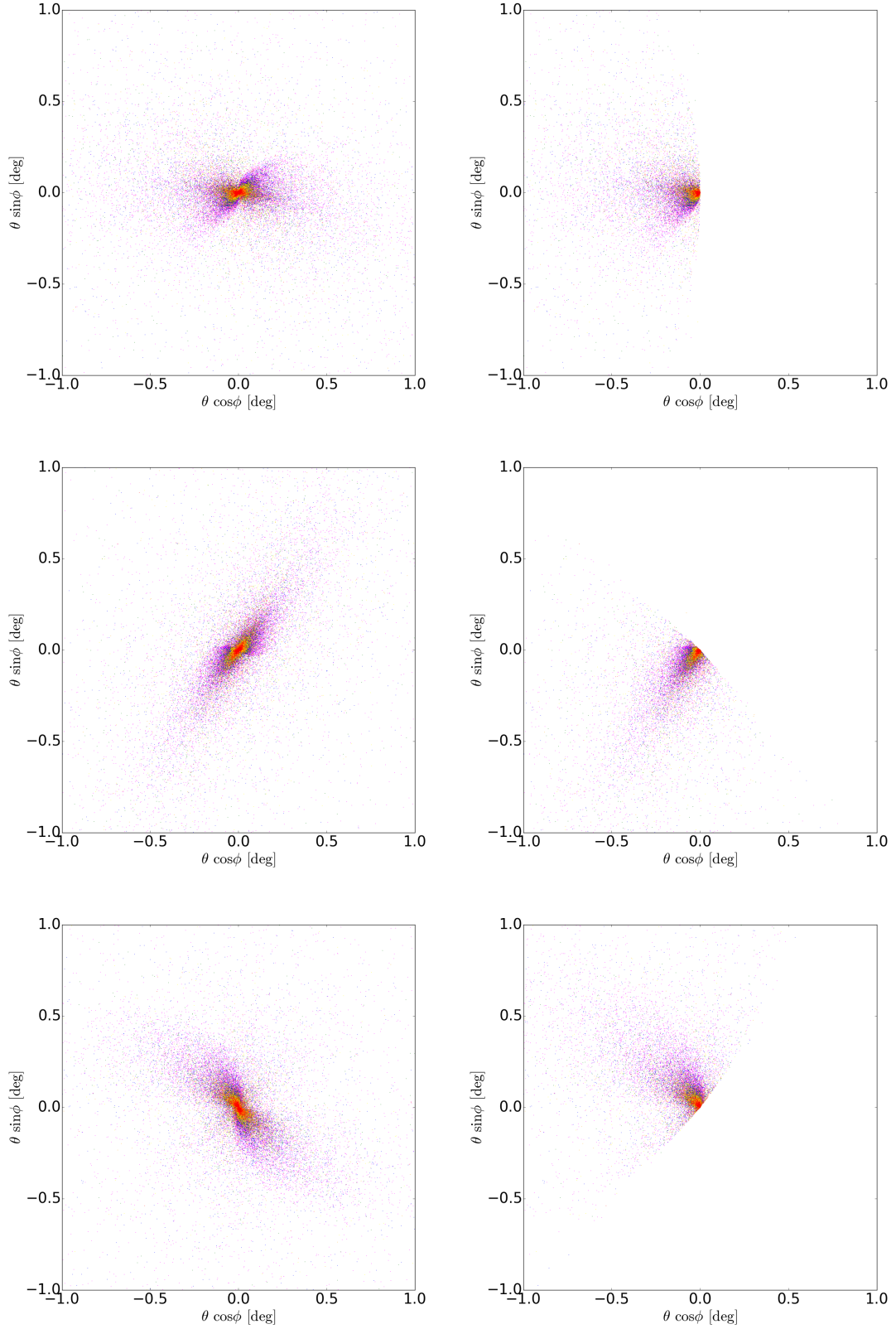


FIG. 3: Sky maps of arrival directions of photons from a blazar at a distance $D_s = 1 \text{ Gpc}$ emitting photons with energy $E_{\text{TeV}} = 10 \text{ TeV}$ in a jet with a half opening angle of $\Psi = 5^\circ$ directed at the observer (left column) and tilted by 5° with respect to the line of sight (right column), respectively. The magnetic field is assumed to be stochastic with RMS strength of $B = 10^{-15} \text{ G}$, coherence length $L_c \simeq 120 \text{ Mpc}$, and maximal negative (upper panels, $f_H = -1$), null (central, $f_H = 0$) and maximal positive (lower panels, $f_H = +1$) helicities, respectively. The colors represent the same energies as in Fig. 2.

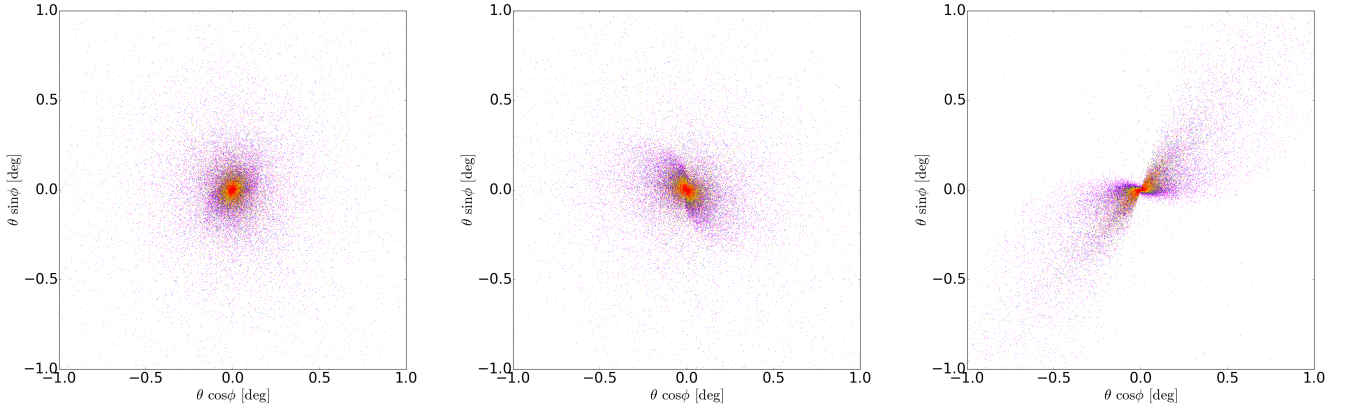


FIG. 4: Sky maps of arrival directions of photons from a blazar at a distance $D_s = 1$ Gpc emitting photons with energy $E_{\text{TeV}} = 10$ TeV in a jet with a half opening angle of $\Psi = 5^\circ$ directed at the observer. The magnetic field is assumed to be stochastic with RMS strength of $B = 10^{-15}$ G and a coherence length of $L_c \simeq 50$ Mpc (left), $L_c \simeq 150$ Mpc (center) and $L_c \simeq 250$ Mpc (right) for $f_H = +1$. The colors represent the same energies as in Fig. 2.

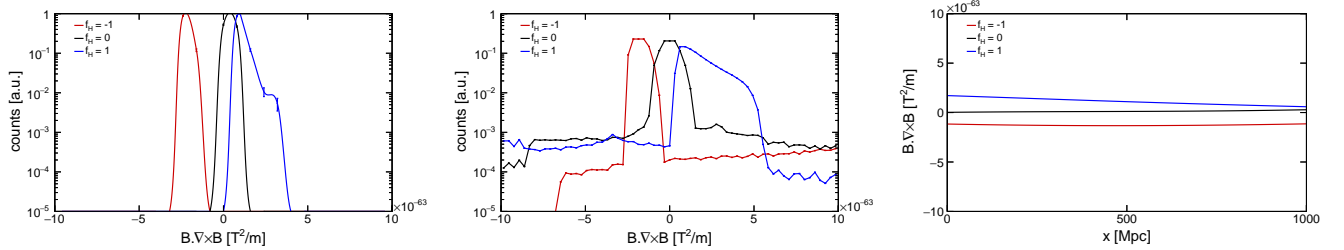


FIG. 5: Different current helicity measures for the three cases shown in Fig. 3, *i.e.* negative current helicity ($f_H = -1$, red), zero current helicity ($f_H = 0$, black) and positive current helicity ($f_H = +1$, blue). The left panel shows the total distribution of “current helicity”, defined as $\mathbf{B} \cdot (\nabla \times \mathbf{B})$ (which serves as a gauge-invariant proxy to the actual magnetic helicity), in the whole simulation box, normalized to 1. In the center panel the same measure is shown, however restricted only to the line of sight and the neighboring cells. Finally, the right panel shows the helicity values along the line of sight from the source (at $x = 0$ Mpc) to the observer (at $x = 1000$ Mpc).

happens close to the source, and both cases have similar helicity measures in that region. As a confirmation of this interpretation we found that in simulations in which the absolute value of $\mathbf{B} \cdot (\nabla \times \mathbf{B})$ is small close to the source, the spiral-like structures tend to be less distinct.

It should be noted, however, that Fig. 5 is depicting the local *current* magnetic helicity, $\mathbf{B} \cdot (\nabla \times \mathbf{B})$, instead of the integrand in the definition of magnetic helicity (Eq. 1), $\mathbf{A} \cdot \mathbf{B}$. The reason for this choice is that while the integral (1) is gauge-invariant and hence the reasonable measure for the overall topological properties of the field [56], $\mathbf{A} \cdot \mathbf{B}$ is *not* gauge-independent and thus cannot be used to plot *local* topological properties. On the other hand, $\mathbf{B} \cdot (\nabla \times \mathbf{B})$ is locally gauge-invariant and consequently a well-defined measure, being an adequate choice to generally describe the local topology.

The sky map containing the arrival directions of gamma rays are shown in Fig. 3. We consider both the case for which the jet is directed along the line of sight (left column) and for which it is tilted by 5° (right column). For the former one can see the impact of magnetic

helicity by comparing the top ($f_H = -1$) and bottom ($f_H = +1$) panels. A remarkable spiral-like pattern is clearly visible, being left- or right-handed depending on whether the helicity is negative or positive, respectively. For zero helicity ($f_H = 0$, middle panels), on the other hand, no clear orientation can be seen.

We show here the results for $L_c \simeq 120$ Mpc. For lower coherence lengths ($L_c \lesssim 50$ Mpc) and $B \lesssim 10^{-15}$ G we find that the arrival direction pattern is washed out, and it is not possible to infer the presence of helicity, thus confirming the analytical predictions of Ref. [41] for this combination of parameters using simulations. This can be seen in Fig. 4 where the results for different L_c and $f_H = +1$ are shown. While for $L_c = 250$ Mpc a clear characteristic spiral in the arrival directions can be seen, it becomes less visible for $L_c = 150$ Mpc and disappears for $L_c = 50$ Mpc. Therefore, $L_c = 120$ Mpc is a reasonable choice in order to show the effects of helicity discussed below. It is also a valid value in certain magnetogenesis scenarios [57].

To understand the dependence of the spiral pattern

on the coherence scale, we note that, for small coherence lengths, the spirals become too tight to be resolved, *i.e.* their angular size becomes too small compared to the overall halo [41]. It seems, however, that the quality of the spiral might be highly sensitive to the specific values of the parameters of the setting such as B , D_s and L_c which we will further investigate in the future.

On the other hand, for larger coherence lengths the spirals tend to a straight line, similarly to the top right panel of Fig. 2, approaching the case of a simple uniform magnetic field. This, again, is rather intuitive, since if $L_c \gtrsim D_s$, the stochastic magnetic field will effectively be uniform on the length scales in question.

On the right hand side of Fig. 3 we show the same scenario described above, but this time the direction of the jet is tilted by 5° with respect to the line of sight. As one can see in the figure, this reduces the effective area of arrival directions and also the symmetry of the pattern. In our example, for instance, one of the “arms” of the spiral pattern or a part of it is removed. This enables us to apply the Q -statistics [39] (discussed below) to relate the helicity of the field with the arrival directions of gamma rays. It should be noted that all findings of this and the previous sections are in good agreement with the analytic predictions of Ref. [41].

D. Computing the Q -factors

One possibility to quantify the role of magnetic helicity is to use the Q -statistics, introduced in Refs. [38–40]. The key elements here are the observed energies and the arrival directions of gamma rays at Earth. For sets of photons with energies E_1 , E_2 and E_3 with $E_1 < E_2 < E_3$, the Q -statistics is given by [39]

$$Q(E_1, E_2, E_3, R) = \frac{1}{N_3} \sum_{j=1}^{N_3} [\boldsymbol{\eta}_{1j}(R) \times \boldsymbol{\eta}_{2j}(R)] \cdot \mathbf{n}_j(E_3), \quad (29)$$

where $\mathbf{n}_j(E_a)$ is the arrival direction of the j -th photon with energy E_a , N_a is the total number of photons of energy E_a , and $\boldsymbol{\eta}_{aj}(R)$ is given by

$$\boldsymbol{\eta}_{aj}(R) \equiv \frac{1}{N_a} \sum_{i \in \mathcal{D}_a(\mathbf{n}_j(E_3), R)} \mathbf{n}_i(E_a), \quad (30)$$

where $\mathcal{D}_a(\mathbf{n}_j(E_3), R)$ represents the set of photons of energy E_a that are located in a disk of radius R centered on $\mathbf{n}_j(E_3)$. Essentially, the Q -statistics is the average value of the triple product of photon arrival vectors of energies E_1, E_2, E_3 that lie within an angle R of the highest energy photon (E_3).

As has been shown in Refs. [38–40], the calculation of the parity-odd statistics, or Q -statistics, should enable us, depending on the sign and general shape of the Q -factors for different values of E_1 , E_2 , E_3 , and R , to draw conclusions about the helicity of the intervening helical magnetic field.

We now use Eq. (29) to calculate the Q -factors for the three helicity scenarios analyzed ($f_H = -1, 0$ and 1). We display the results for the case of tilted jets (*i.e.* the scenario shown in the right panel of Fig. 3) in Fig. 6. We consider triplets of energies (E_1, E_2, E_3) as needed for Eq. (29), where each energy E_i corresponds to an interval $[E_i, E_i + 10 \text{ GeV}]$.

The reason we consider the scenario of *tilted* jets is that this is the most probable case – it is very unlikely for the blazar jet to be directed exactly along the line of sight. As discussed in Ref. [40], the function $Q(R)$ is expected to start at the origin since the angular deflections are small for small R . For larger R , the magnetic helicity causes Q to grow, and at much larger R , Q will approach a constant value (Q_∞) as there are no more photons to include at such large R . The large R behavior gets modified in a realistic setting where, in addition to the blazar photons, we also observe background photons from other sources. Then, for large R , the blazar contribution gets diluted by the background noise and Q decreases to zero. In this case, we would see a peak in $Q(R)$ whose position is set by the relative number of blazar to background photons. In our simulations, however, we do not include background photons and indeed find $Q \rightarrow Q_\infty$ at large R .

E. Computing the S -Statistics

As the last part of our results we present a new alternative way to quantify the pattern of gamma ray arrival directions and thus, indirectly, the helicity orientation. The idea underlying idea of this new method that we denote S -Statistics (for “Spiral”) is that a gamma ray from a cascade that has a greater deflection away from the source direction due to the magnetic field will also have a greater azimuthal deflection if the magnetic field is helical. The pattern of observed gamma rays will have a spiral structure that can be measured by finding the average deflection of gamma rays, $\bar{\theta}(\phi, E_\gamma)$, as a function of the azimuthal angle ϕ and the considered gamma ray energy E_γ . We assume that there is at least one angle ϕ_{\max} for which $\bar{\theta}(\phi, E_\gamma)$ has a well-defined and significant maximum, *i.e.* a maximum from an average in a bin which has a reasonable number of photons *and* is statistically significant. We consider events inside a band around ϕ_{\max} with width $2\Delta\phi$, *i.e.* events with $\phi_{\max} - \Delta\phi \leq \phi \leq \phi_{\max} + \Delta\phi$. For a right-handed spiral there should be higher values of $\bar{\theta}(\phi, E_\gamma)$ for $\phi < \phi_{\max}$ than for $\phi > \phi_{\max}$ inside the band, while for a left-handed pattern $\bar{\theta}(\phi, E_\gamma)$ should be smaller for $\phi < \phi_{\max}$ than for $\phi > \phi_{\max}$. In other words, the peak of the function $\bar{\theta}(\phi)$ should be skewed to the right or to the left depending on whether the spiral is right- or left-handed, respectively. By finding a measure for this asymmetry or skew of the maximum one can deduce the orientation and subsequently the magnetic helicity.

More concretely, the calculation is performed in the following way: first, we subdivide the interval on which

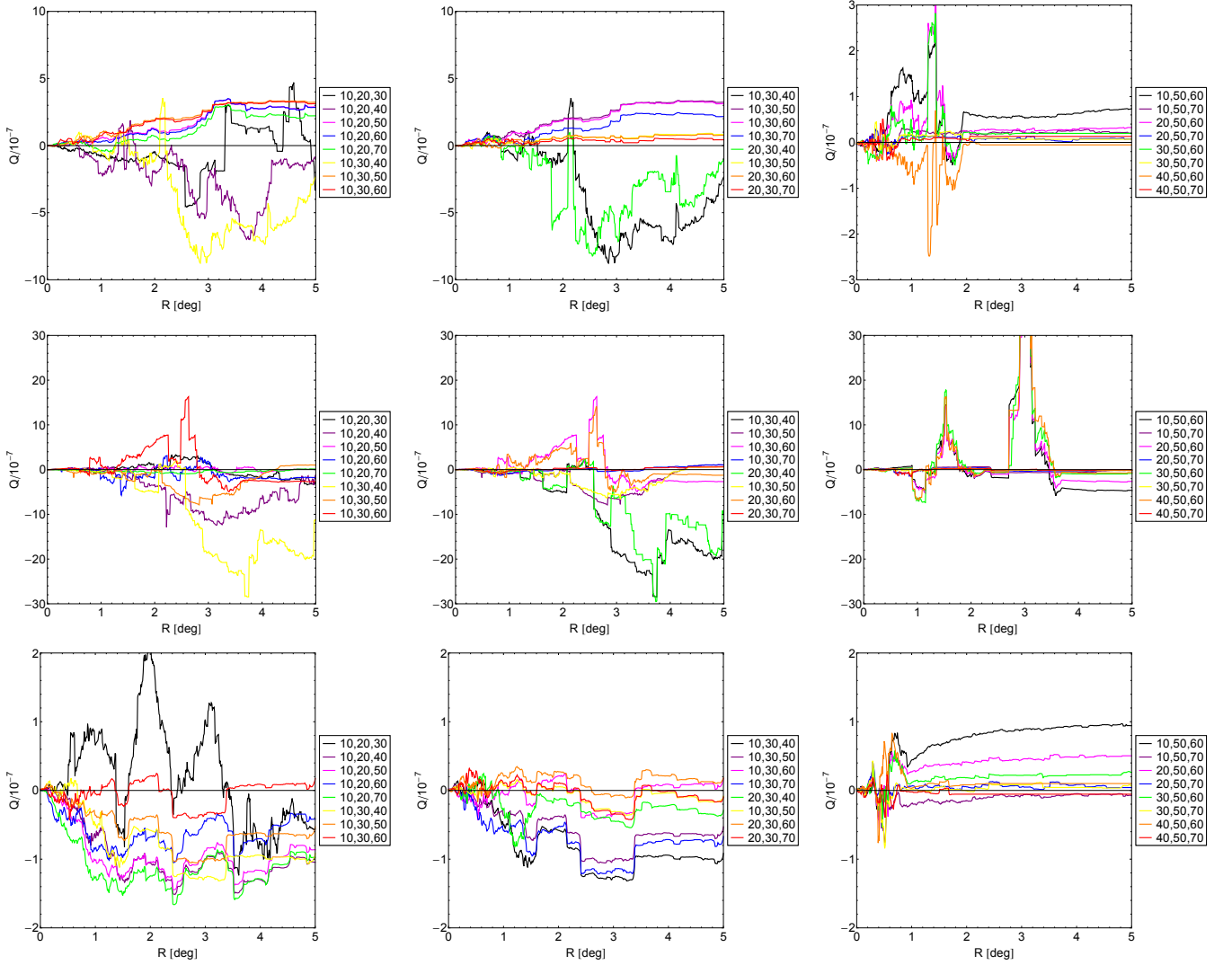


FIG. 6: Q -statistics for the case of a source tilted 5° with respect to the line of sight, for $D_s = 1$ Mpc, $E_{\text{TeV}} = 10$ TeV and $\Psi = 5^\circ$. All panels correspond to the three right hand panels of Fig. 3, *i.e.* $f_H = -1$ at the top, $f_H = 0$ in the middle $f_H = +1$ at the bottom panel. The triplets in the legends correspond to E_1, E_2, E_3 in GeV, each in intervals of $[E_i, E_i + 10 \text{ GeV}]$.

ϕ is defined, *i.e.* $\phi \in [0, 2\pi)$, in n_{bin} bins, such that each of the bins has a width $\delta\phi = 2\pi/n_{\text{bin}}$. The j th bin, which corresponds to the interval $[(j-1)\delta\phi, j\delta\phi)$, $j = 1, \dots, n_{\text{bin}}$, will be labeled $\phi^{(j)} = (j-1)\delta\phi$. For each bin we calculate $\bar{\theta}$ by

$$\bar{\theta}(\phi^{(j)}, E_\gamma) = \frac{1}{N_j} \sum_{\{i | \phi^{(j)} \leq \phi_i < \phi^{(j+1)}\}} \theta_i, \quad (31)$$

where (ϕ_i, θ_i) are the coordinates of the i th event in the set $\{i | \phi^{(j)} \leq \phi_i < \phi^{(j+1)}\}$ and N_j is the total number of events in this set. If $\{i | \phi^{(j)} \leq \phi_i < \phi^{(j+1)}\}$ is empty, we set $\bar{\theta}(\phi^{(j)}, E_\gamma) = 0$. Furthermore, for real data it might be necessary to restrict the analysis to events with θ smaller than a certain value θ_{max} as for $\theta > \theta_{\text{max}}$ background photons might dominate and result in a false signal.

In this set of $\bar{\theta}(\phi^{(j)}, E_\gamma)$ one now has to identify the relevant and significant maxima as well as the corresponding bin number j_{max} and calculate the quantities

$$\Phi_- = \sum_{j=j_{\text{max}}-\delta_{\text{bin}}}^{j_{\text{max}}-1} \bar{\theta}(\phi^{(j)}, E_\gamma), \quad \Phi_+ = \sum_{j=j_{\text{max}}+1}^{j_{\text{max}}+\delta_{\text{bin}}} \bar{\theta}(\phi^{(j)}, E_\gamma), \quad (32)$$

where $\delta_{\text{bin}} \geq 1$ is the number of bins we need to consider in order to include the width of the peak. Here one has to assume periodicity, *i.e.* $\bar{\theta}(\phi^{(j+n_{\text{bin}})}) = \bar{\theta}(\phi^{(j)}, E_\gamma)$. Essentially Φ_- corresponds to the average value of θ to the left of the peak and Φ_+ to the right of the peak.

The final step is to define the S -statistics that measures the skewness of the peak

$$S \equiv \frac{\Phi_- - \Phi_+}{\Phi_- + \Phi_+} \quad (33)$$

For a right-handed spiral S will be positive, whereas for a left-handed spiral it will be negative.

We performed this computation for the data shown in Fig. 3. The plots for $\theta(\phi, E_\gamma)$, shown for different energies, are presented in Fig. 7. Even without any further analysis one can see in this figure that the peaks for opposite orientations indeed show opposite skews – while on the left panel higher angles are achieved for $\phi > \phi_{\max}$, on the right panel, even more clearly, that is the case for $\phi > \phi_{\max}$. For the central panel, however, peaks of either skewness are found.

In order to support these qualitative considerations, one has to look at the S -values which have been calculated and are presented for the three cases in Tabs. I–III. The most clear case here is the one for $f_H = -1$, where for all energy ranges we obtain $S < 0$ with two values even going as low as $S \simeq -0.5$. This means that the morphology of the arrival directions is solely right-handed which is also clearly seen in the top panel of Fig. 3. For the case of $f_H = +1$ the situation is less clear as there is only one value being as high as $S \simeq +0.48$. Nevertheless, since S is positive for all energy ranges with three exceptions for which, however the absolute value of S is close to zero, this is strong evidence for a left-handed orientation. Finally, no clear statement can be made regarding the case with no helicity ($f_H = 0$) – here one does not find significant negative or positive values for S . It should be noted that here only a measurement for a single source is presented, however, in order to make a strong statement, for better statistics, data from several sources has to be analyzed. In this way, the S -statistics for $f_H = 0$, which is less clear than for the other two cases, may be seen as an example for how such a single source approach may not be enough to make a final decision.

As the last step, we need to connect the handedness of the arrival direction pattern with the sign of helicity. Their correlation has been found in Ref. [41], where an analysis has been carried out for a homogeneous magnetic field. In this reference the authors indeed find that for a positive helicity one expects a right-handed orientation, whereas for negative helicities a left-handed orientation should be observed, thus confirming our results for stochastic fields.

As a concluding remark it should be stated that for the results presented above we used simulations containing approximately 1.4×10^5 photons arriving at Earth in the energy range $1.5 \leq E_\gamma/\text{GeV} \leq 100$, which provided clear patterns with satisfactory statistical significance. The upcoming Cherenkov Telescope Array (CTA) [58] might be able to detect this kind of signature in the energy range $E \simeq 10 - 100$ GeV with $\gtrsim 10$ hours of observation. Fewer photons would distort the picture since, for example in the case of the S -statistics, the peaks would become less visible, such that a reliable calculation would no longer be possible. This is the case for high energy photons as their contribution to the total flux is rather small. On the other hand, for the lowest energies (\sim a few GeV), even with as few as 10^4 photons relevant peaks

TABLE I: Table for S for maximal negative helicity ($f_H = -1$).

E_γ/GeV	j_{\max}	ϕ_{\max}/deg	Φ_-	Φ_+	S
5–10	6	108.0	0.768	1.67	-0.37
	16	288.0	0.649	1.60	-0.42
10–15	7	126.0	0.813	0.904	-0.05
	17	306.0	0.709	0.882	-0.11
15–20	7	126.0	0.472	0.818	-0.27
	18	324.0	0.637	0.473	0.15
20–30	6	108.0	0.222	0.625	-0.48
	17	306.0	0.370	0.428	-0.07
30–50	6	108.0	0.163	0.507	-0.51
	16	288.0	0.170	0.385	-0.39
50–100	7	126.0	0.151	0.200	-0.13
	17	306.0	0.145	0.172	-0.09

TABLE II: Table for S for vanishing helicity ($f_H = 0$).

E_γ/GeV	j_{\max}	ϕ_{\max}/deg	Φ_-	Φ_+	S
5–10	4	72.0	1.69	12.12	-0.11
	17	306.0	2.99	1.69	+0.28
10–15	6	108.0	1.80	1.04	+0.27
	17	306.0	2.21	1.28	+0.27
15–20	5	90.0	1.12	1.07	+0.02
	13	234.0	1.01	1.28	-0.12
20–30	6	108.0	1.02	0.610	+0.25
	16	288.0	1.07	0.608	+0.28
30–50	4	72.0	0.463	0.470	-0.01
	14	252.0	0.491	0.511	-0.02
50–100	4	72.0	0.277	0.275	+0.00
	16	288.0	0.418	0.218	+0.31

can be seen, which, however, might be more difficult to construe in a more realistic case considering additionally diffuse gamma ray radiation and multiple sources.

IV. DISCUSSION AND OUTLOOK

We have performed three-dimensional Monte Carlo studies of the development of gamma-ray-induced electromagnetic cascades in the intergalactic medium in the presence of magnetic fields. We have used the “Large Sphere Observer” method for improved computational performance. In this case all cascade photons hitting the surface of the sphere are detected by the observer. With a standard three-dimensional Monte Carlo simulation most cascade photons would not reach Earth, resulting in wasted computation and very low statistics. A simplification made in our treatment is that the magnetic field evolves adiabatically with redshift as $B(z) = B(z=0)(1+z)^2$. This is justified because the

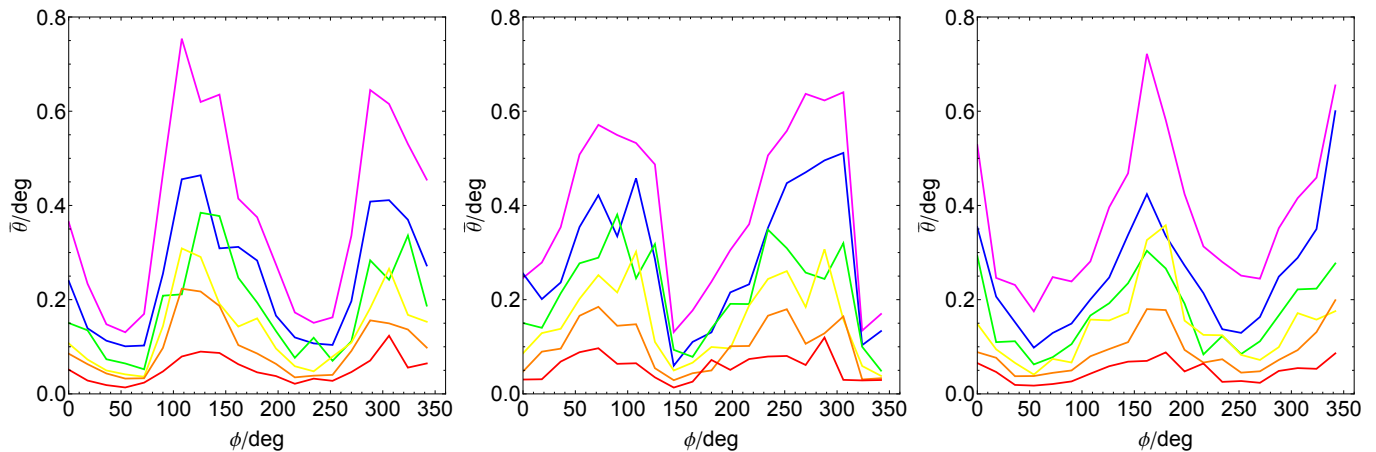


FIG. 7: The average polar angle $\bar{\theta}$ in dependence on the azimuthal angle ϕ , as calculated in (31) for the three cases $f_H = -1$ (left), $f_H = 0$ (center) and $f_H = +1$ (right), corresponding to the three cases in Fig. 3. Here we have chosen $n_{\text{bin}} = 20$. The colors correspond to the energy ranges of the arrival energies E_γ in the same way as in Fig. 2, *i.e.* 5 – 10 GeV (magenta), 10 – 15 GeV (blue), 15 – 20 GeV (green), 20 – 30 GeV (yellow), 30 – 50 GeV (orange), 50 – 100 GeV (red).

TABLE III: Table for S for maximal positive helicity ($f_H = +1$).

E_γ/GeV	j_{max}	$\phi_{\text{max}}/\text{deg}$	Φ_-	Φ_+	S
5–10	19	342.0	1.23	1.01	+0.10
	9	162.0	1.15	1.32	-0.07
10–15	19	342.0	0.888	0.713	+0.11
	9	162.0	0.785	0.822	-0.02
15–20	0	0.0	0.722	0.284	+0.44
	9	162.0	0.594	0.542	+0.05
20–30	19	342.0	0.428	0.309	+0.16
	10	180.0	0.655	0.405	+0.24
30–50	19	342.0	0.296	0.203	+0.19
	9	162.0	0.285	0.338	-0.08
50–100	19	342.0	0.157	0.131	+0.09
	10	180.0	0.120	0.138	+0.18

cascade development we have discussed occurs in cosmic voids where MHD amplification and contamination by sources is minimal. Also, the sources are at redshifts $z \lesssim 1$.

We first compared our computational setup with analytical approximations and then validated it in simple scenarios containing a uniform magnetic field oriented parallelly and perpendicularly to the line of sight of the blazar jet. As expected, for a magnetic field parallel to the direction of the jet of half-opening angle Ψ , assumed to be pointing toward Earth, effects of the field were not observed. For a magnetic field perpendicular to the direction of the jet, deflections were non-zero and in the expected direction. Similar results were obtained for stronger and weaker magnetic fields and other orientations. These results are in accordance with Ref. [41] and also with the predictions of Eq. (26).

We have also studied the particular case of a magnetic field with a Batchelor power spectrum with and without helicity. The effects of helicity can be clearly seen in Fig. 3, where arrival directions follow right- or left-handed spirals, depending on the sign of the helicity. For stochastic fields, in general, the results tend to converge toward the case of a uniform magnetic field in the limit of large coherence lengths. We have considered only large values of correlation length ($L_c \simeq 120$ Mpc) since for much smaller coherence lengths, with the other parameters being held fixed, no clear signature of helicity can be seen, as shown in Fig. 4. Nevertheless, one should bear in mind that the current upper limits of coherence length of magnetic fields in voids range between a few and hundreds of Mpc [57], placing the chosen value of 120 Mpc well within the allowed bounds.

We have deployed the so-called Q -statistics, a powerful analysis tool that makes it possible to determine the properties of magnetic helicity directly from the observables of gamma rays measured at Earth. In this work we for the first time applied Q -statistics to realistic three-dimensional simulations of electromagnetic cascades. Our results for Q are shown in Fig. 6. The plots do not show a strong correlation between Q and the existence and sign of the helicity. At the moment we cannot clearly state whether averaging over several objects will show a stronger correlation. We plan on investigating this issue in a future work.

It is important to stress the fact that Q -statistics might not be the final method to quantify magnetic helicity, however it is a good initial approach and has been used in several works (Refs. [38, 39, 41]) with satisfactory results. In this work we have, for the first time, introduced the S -statistics, which is a direct measure of the handedness of a pattern with respect to the line of sight. We have shown that the orientation, represented by the sign of S , is directly correlated with the sign of helicity. This shows

that the S measure is also a powerful tool to be used in the analysis of helicity of IGMF, even though only once several sources have been measured, a clear statement on the overall helicity may be made.

Backgrounds at the ~ 10 -100 GeV energy range are expected due to secondary photons from AGN halos whose jet opening angles do not encompass the Earth. Other astrophysical sources of photons in this energy range also exist and have to be taken into account. In this first work we have neglected these backgrounds, which will be included in future studies.

We found that it is probably necessary to analyze various sources in order to make a definite statement about the sign of the helicity, since a clear signature cannot always be seen. In the future we will extend our simulations to the case of multiple sources and diffuse gamma rays. We expect to be able to reproduce actual detections and consequently retrieve more precise information about IGMF, which can be used to infer their origin and evolution.

In addition, we will extend the analysis by further exploring the parameter space as varying quantities such as the magnetic field strength B_{rms} , the magnetic correlation length L_c and source parameters such as its distance from the observer, its energy spectrum or its cutoff energy, as they may be important in order to obtain a complete picture of their influence as discussed above and to explain actual observations.

Acknowledgments

R. A. B. acknowledges the financial support from the John Templeton Foundation. The work of A. S. has been supported by the DAAD funded by the BMBF and the

EU Marie Curie Actions. A. S. would like to thank the Arizona State University for the hospitality during his stay. Furthermore, A. S. is grateful to the "Helmholtz Alliance for Astroparticle Physics" (HAP) and the Collaborative Research Center SFB 676 "Particles, Strings and the Early Universe" for providing generous travel funds which were important for the collaboration leading to this work. T. V. is supported by DOE, Office of High Energy Physics, under Award number #DE-SC0013605 at ASU. T. V. is grateful to the Institute for Advanced Study, Princeton for hospitality while this work was being done. Special thanks go to Andrew J. Long for his ideas and discussions which helped to complete this work and to NORDITA in Stockholm for organizing the workshop "Origin, Evolution, and Signatures of Cosmological Magnetic Fields" during which important aspects of this work have been discussed.

Appendix A: Relating Current Helicity to the other Helicity Measures

In this section we want to derive the connection between the correlator of magnetic fields and the current helicity which is the main local observable for the topology of magnetic fields. Following [59] we are starting with the correlator for a magnetic field,

$$\langle B_i(\mathbf{x})B_j(\mathbf{x}+\mathbf{r}) \rangle = M_N(r)P_{ij} + M_L\frac{r_i r_j}{r^2} + \epsilon_{ijl}\frac{r_l}{r}M_H(r) \quad (\text{A1})$$

where $P_{ij} = \delta_{ij} - r_i r_j / r^2$ and furthermore M_N , M_L and M_H is the normal, longitudinal and, most important for us, the helical power spectrum, respectively.

On the other hand, the correlator (in Coulomb Gauge) for an isotropic magnetic field is given by [59]

$$\langle \tilde{B}_m(\mathbf{k})\tilde{B}_n^*(\mathbf{k}') \rangle = (2\pi)^6 \delta^{(3)}(\mathbf{k}-\mathbf{k}') \left[\frac{E_B(k)}{k^3} \left(\delta_{mn} - \frac{k_m k_n}{k^2} \right) - i\epsilon_{mnl}k_l \frac{H_B(k)}{8\pi k^3} \right], \quad (\text{A2})$$

where E_B and H_B are the quantities defined in (17) and (18), respectively. Combining (A1) with (A2) gives (for the helical part) the dependence between the helicity densities $H_B(k)$ and $M_H(r)$ in Fourier and real space, respectively:

$$M_H = \frac{1}{2} \int H_B \frac{d}{d(kr)} \left[\frac{\sin(kr)}{kr} \right] dk. \quad (\text{A3})$$

This is the crucial statement of this section as it shows how to obtain a real space helicity measure from its spectral counterpart. The last step is to show how current

helicity is connected to those. To do so we simply calculate the correlator $\langle \mathbf{B}(\mathbf{x}) \cdot [\nabla \times \mathbf{B}(\mathbf{x})] \rangle$ which can be done using (A2) and gives

$$\langle \mathbf{B}(\mathbf{x}) \cdot [\nabla \times \mathbf{B}(\mathbf{x})] \rangle = - \int k^2 H_B(k) d \ln k \quad (\text{A4})$$

From this relation one can see that similar to the helicity term $\mathbf{A} \cdot \mathbf{B}$ also the current helicity $\mathbf{B} \cdot [\nabla \times \mathbf{B}]$ may be used to obtain the spectral helicity H_B and thus, with (A3), the overall magnetic helicity.

-
- [1] M. S. Turner and L. M. Widrow, *Phys. Rev. D* **37**, 2743 (1988).
- [2] B. Ratra, *Astrophys. J.* **391**, L1 (1992).
- [3] C. T. Byrnes, L. Hollenstein, R. K. Jain, and F. R. Urban, *J. Cosmol. Astropart. Phys.* **1203**, 009 (2012).
- [4] R. J. Z. Ferreira, R. K. Jain, and M. S. Sloth, *J. Cosmol. Astropart. Phys.* **1406**, 053 (2014).
- [5] T. Vachaspati, *Phys. Lett. B* **265**, 258 (1991).
- [6] K. Enqvist and P. Olesen, *Phys. Lett. B* **319**, 178 (1993).
- [7] G. Baym, D. Bödeker, and L. McLerran, *Phys. Rev. D* **53**, 662 (1996).
- [8] D. Grasso and A. Riotto, *Phys. Lett. B* **418**, 258 (1998).
- [9] C. J. Hogan, *Phys. Rev. Lett.* **51**, 1488 (1983). doi:10.1103/PhysRevLett.51.1488
- [10] J. M. Quashnock, A. Loeb, and D. N. Spergel, *Astrophys. J. Lett.* **344**, L49 (1989).
- [11] G. Sigl, A. V. Olinto, and K. Jedamzik, *Phys. Rev. D* **55**, 4582 (1997).
- [12] A. G. Tevzadze, L. Kisslinger, A. Brandenburg, and T. Kahniashvili, *Astrophys. J.* **759**, 54 (2012).
- [13] A. J. Long, E. Sabancilar, and T. Vachaspati, *J. Cosmol. Astropart. Phys.* **1402**, 036 (2014).
- [14] A. J. Long and E. Sabancilar, *J. Cosmol. Astropart. Phys.* **1605**, 029 (2016).
- [15] R. M. Kulsrud, R. Cen, J. P. Ostriker, and D. Ryu, *Astrophys. J.* **480**, 481 (1997).
- [16] D. A. Leahy and A. Vilenkin, *Astrophys. J.* **248**, 13 (1981).
- [17] S. Bertone, C. Vogt, and T. Enßlin, *Mon. Not. R. Astron. Soc.* **370**, 319 (2006).
- [18] J. Donnert, K. Dolag, H. Lesch, and E. Muller, *Mon. Not. R. Astron. Soc.* **392**, 1008 (2009).
- [19] A. Neronov and D. V. Semikoz, *Phys. Rev. D* **80**, 123012 (2009).
- [20] A. Neronov and D. V. Semikoz, *JETP Lett.* **85**, 473 (2007).
- [21] W. Essey, S. Ando, and A. Kusenko, *Astropart. Phys.* **35**, 135 (2011).
- [22] S. Ando and A. Kusenko, *Astrophys. J. Lett.* **722**, L39 (2010).
- [23] F. Tavecchio *et al.*, *Mon. Not. R. Astron. Soc.* **406**, L70 (2010).
- [24] A. M. Taylor, I. Vovk, and A. Neronov, *Astron. Astrophys.* **529**, A144 (2011).
- [25] K. Takahashi *et al.*, *Astrophys. J.* **771**, L42 (2013).
- [26] W. Chen, J. H. Buckley, and F. Ferrer, *Phys. Rev. Lett.* **115**, 211103 (2015).
- [27] A. E. Broderick, P. Chang, and C. Pfrommer, *Astrophys. J.* **752**, 22 (2012).
- [28] R. Schlickeiser, D. Ibscher, and M. Supsar, *Astrophys. J.* **758**, 102 (2012).
- [29] R. Schlickeiser, S. Krakau, and M. Supsar, *Astrophys. J.* **777**, 49 (2013).
- [30] A. Saveliev, C. Evoli, and G. Sigl, arXiv:1311.6752 [astro-ph.HE] (2013).
- [31] P. Chang *et al.*, *Astrophys. J.* **797**, 110 (2014).
- [32] W. Chen *et al.*, *Mon. Not. R. Astron. Soc.* **450**, 3371 (2015).
- [33] L. Sironi and D. Giannios, *Astrophys. J.* **787**, 49 (2014).
- [34] G. Sigl, *Phys. Rev. D* **66**, 123002 (2002).
- [35] A. Alexakis, P. D. Mininni, and A. Pouquet, *Astrophys. J.* **640**, 335 (2006).
- [36] A. Saveliev, K. Jedamzik, and G. Sigl, *Phys. Rev. D* **87**, 123001 (2013).
- [37] T. Kahniashvili and T. Vachaspati, *Phys. Rev. D* **73**, 063507 (2006).
- [38] H. Tashiro and T. Vachaspati, *Phys. Rev. D* **87**, 123527 (2013).
- [39] H. Tashiro, W. Chen, F. Ferrer, and T. Vachaspati, *Mon. Not. R. Astron. Soc.* **445**, L41 (2013).
- [40] H. Tashiro and T. Vachaspati, *Mon. Not. R. Astron. Soc.* **448**, 299 (2015).
- [41] A. J. Long and T. Vachaspati, *J. Cosmol. Astropart. Phys.* **1509**, 065 (2015).
- [42] T. Vachaspati, *Phys. Rev. Lett.* **87**, 251302 (2001).
- [43] C. Caprini and L. Sorbo, *J. Cosmol. Astropart. Phys.* **1410**, 056 (2014).
- [44] F. Aharonian, P. S. Coppi, and H. J. Völk, *Astrophys. J. Lett.* **423**, L5 (1994).
- [45] R. Plaga, *Nature* **374**, 430 (1994).
- [46] R. Alves Batista *et al.*, *J. Cosmol. Astropart. Phys.* **1605**, 038 (2016).
- [47] M. Kachelrieß, S. Ostapchenko, and R. Tomàs, *Comp. Phys. Commun.* **183**, 1036 (2012).
- [48] J. M. Jauch and F. Rohrlich, *The Theory of Photons and Electrons. The Relativistic Quantum Field Theory of Charged Particles with Spin One-Half*, 2nd ed. (Springer, New York, 1976).
- [49] T. M. Kneiske and H. Dole, *Astron. Astrophys.* **515**, A19 (2010).
- [50] H. Tashiro, T. Vachaspati, and A. Vilenkin, *Phys. Rev. D* **86**, 105033 (2012).
- [51] A. Brandenburg and K. Subramanian, *Phys. Rep.* **417**, 1 (2005).
- [52] T. Kahniashvili, A. G. Tevzadze, A. Brandenburg, and A. Neronov, *Phys. Rev. D* **87**, 083007 (2013).
- [53] A. Elyiv, A. Neronov, and D. V. Semikoz, *Phys. Rev. D* **80**, 023010 (2009).
- [54] A. Neronov *et al.*, *Astrophys. J. Lett.* **719**, L130 (2010).
- [55] D. Harari, S. Mollerach, E. Roulet, and F. Sanchez, *J. High Energy Phys.* **03**, 045 (2002).
- [56] M. A. Berger and G. B. Field, *J. Fluid Mech.* **147**, 133 (1984).
- [57] R. Durrer and A. Neronov, *Astron. Astrophys. Rev.* **21**, 1 (2013).
- [58] B. S. Acharya *et al.*, *Astropart. Phys.* **43**, 3 (2013).
- [59] T. Vachaspati, arXiv:1606.06186 [astro-ph.CO].